

# Weak lensing analysis of RXC J2248.7-4431

D. Gruen<sup>1,2\*</sup>, F. Brimiouille<sup>1,2</sup>, S. Seitz<sup>1,2</sup>, C.-H. Lee<sup>1,2</sup>, J. Young<sup>3</sup>, J. Koppenhoefer<sup>1,2</sup>, T. Eichner<sup>1,2</sup>, A. Riffeser<sup>1,2</sup>, V. Vikram<sup>4</sup>, T. Weidinger<sup>1,2</sup>, A. Zenteno<sup>1</sup>

<sup>1</sup> *University Observatory Munich, Scheinerstrasse 1, 81679 Munich, Germany*

<sup>2</sup> *Max Planck Institute for Extraterrestrial Physics, Giessenbachstrasse, 85748 Garching, Germany*

<sup>3</sup> *Ohio State University, Department of Physics, 191 West Woodruff Avenue, Columbus, Ohio 43210*

<sup>4</sup> *Department of Physics and Astronomy, University of Pennsylvania, 209 South 33<sup>rd</sup> Street, Philadelphia, PA 19104, USA*

## ABSTRACT

We present a weak lensing analysis of the cluster of galaxies RXC J2248.7-4431, a massive system at  $z = 0.3475$  with prominent strong lensing features covered by the HST/CLASH survey (Postman et al. 2012). Based on UBVRIZ imaging from the WFI camera at the MPG/ESO-2.2m telescope, we measure photometric redshifts and shapes of background galaxies. The cluster is detected as a mass peak at  $5\sigma$  significance. Its density can be parametrised as an NFW profile (Navarro et al. 1996) with two free parameters, the mass  $M_{200m} = 33.1^{+9.6}_{-6.8} \cdot 10^{14} M_{\odot}$  and concentration  $c_{200m} = 2.6^{+1.5}_{-1.0}$ . We discover a second cluster inside the field of view at a photometric redshift of  $z \approx 0.6$ , with an NFW mass of  $M_{200m} = 4.0^{+3.7}_{-2.6} \cdot 10^{14} M_{\odot}$ .

**Key words:** galaxies: clusters: individual: RXC J2248.7-4431; gravitational lensing: weak; gravitational lensing: strong; cosmology: dark matter

## 1 INTRODUCTION

Clusters of galaxies, such as RXC J2248.7-4431 (cf. Figure 1) studied in this work, are the most massive gravitationally bound objects that have formed in the universe until today. What makes them interesting for cosmology is that they lie at an intersection of the two potentially most important unresolved questions: their mass content is dominated by Dark Matter - and their formation and evolution is strongly influenced by the interplay of matter density and Dark Energy. For this reason, studying clusters of galaxies is also a powerful probe of cosmological parameters and models (e.g. Wang & Steinhardt 1998; Holder et al. 2001; Weller et al. 2002).

Perhaps the most important property of a cluster of galaxies with respect to cosmology is its virial mass, which can be determined in several different ways. The number and the velocity dispersion of cluster member galaxies are related to the total mass of the system. One can use larger fractions of the overall mass as a proxy by observing the hot intra-cluster gas, which emits X-ray radiation (e.g. Böhringer et al. 2004; Sahlen et al. 2009; Piffaretti et al. 2011) and changes the cosmic microwave background spectrum due to inverse Compton scattering (Sunyaev-Zel'dovich (SZ) effect, cf. Sunyaev & Zel'dovich

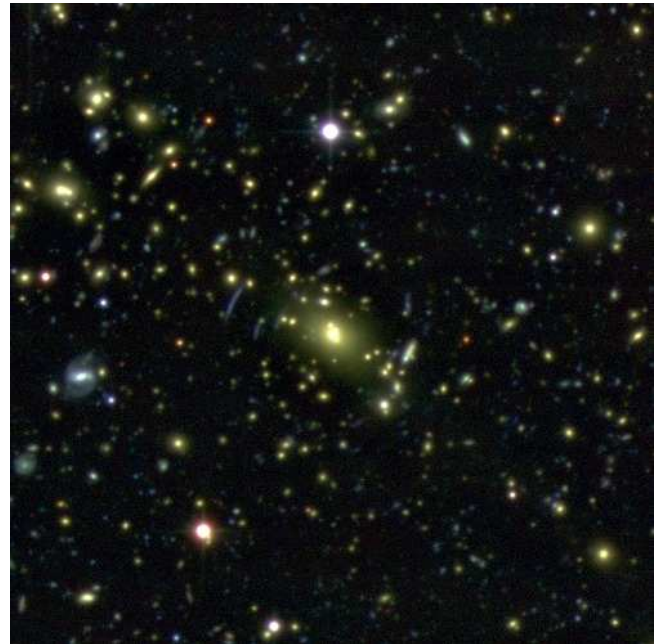


**Figure 1.** BRI colour image of the central 200x200 arcsec of RXC J2248.7-4431. Clearly visible are the brightest cluster galaxy and several gravitational arcs, along with a high concentration of yellow cluster member galaxies.

\* E-mail: dgruen@usm.uni-muenchen.de (DG)

1972; Haiman et al. 2001; Battye & Weller 2003). The latter observables can be related to mass by astrophysical modelling or self-calibration (Hu 2003; Majumdar & Mohr 2004).

Despite this, however, weak gravitational lensing is a valuable ingredient since the tangential alignment of background galaxy images is directly proportional to overdensity of all cluster matter - luminous or dark - alike and is insensitive to the astrophysical state of the cluster. This allows for unbiased mass measurements of single clusters and improved calibration of other mass-observable relations (e.g. Allen et al. 2002; Okabe et al. 2010; Hoekstra et al. 2011). Furthermore, gravitational lensing straightforwardly allows the probing of additional properties of the density profiles of dark matter haloes, such as their concentrations, for which predictions in a cosmological model can be made and from which additional constraints can be drawn (see for instance the Cluster Lensing And Supernova survey with Hubble (CLASH), in which RXC J2248.7-4431 is also observed, cf. Postman et al. 2012).

In this work we analyse the weak lensing effect of the cluster RXC J2248.7-4431 based on background galaxy shapes and photometric redshifts measured from UBVRIZ multi-band imaging by the Wide-Field Imager (WFI) on the 2.2m MPG/ESO telescope at La Silla. In Section 2, we introduce the basic properties of the data used and our data reduction. Section 3 summarises previous optical, X-ray and SZ observations of RXC J2248.7-4431. We give an overview of the photometric analysis, including photometric redshifts, cluster member photometry and morphology in Section 4. Technical aspects of our weak lensing measurements are discussed in Section 5. The analysis of the weak lensing effect of RXC J2248.7-4431 is presented in Section 6. Results for a second cluster found in the field of view at  $z \approx 0.6$  are shown in Section 7. We summarise our results in Section 8.

All numerical values given in this work are calculated for cosmological parameters  $H_0 = 72 \text{ km s}^{-1} \text{ Mpc}^{-1}$  and  $\Omega_m = 1 - \Omega_\Lambda = 0.27$ . Where applicable, measurements from the literature have been converted to this cosmology as well. We denote the radii of spheres around the cluster centre with fixed overdensity as  $r_{\Delta m}$  and  $r_{\Delta c}$ , where  $\Delta$  is the overdensity factor of the sphere with respect to the mean matter density  $\rho_m$  or critical density  $\rho_c$  of the universe at the cluster redshift. Masses inside these spheres are labelled and defined correspondingly as  $M_{\Delta m} = \Delta \cdot \frac{4\pi}{3} r_{\Delta m}^3 \cdot \rho_m$  and  $M_{\Delta c} = \Delta \cdot \frac{4\pi}{3} r_{\Delta c}^3 \cdot \rho_c$ .

## 2 OBSERVATIONS AND DATA REDUCTION

This analysis is based on observations made with the Wide-Field Imager (WFI) on the 2.2m MPG/ESO telescope at La Silla. The sensitivity of the instrument and the filters available spans all optical wavelengths and with its field of view of  $33 \times 33$  arcmin it is well suited for weak lensing cluster analyses with photometric redshifts.

The observations in U (#877), B (#842), V (#843), R (#844), I (#879) and Z (#846) band<sup>1</sup> used in this work were taken in the years 2009-2010. Details of integration

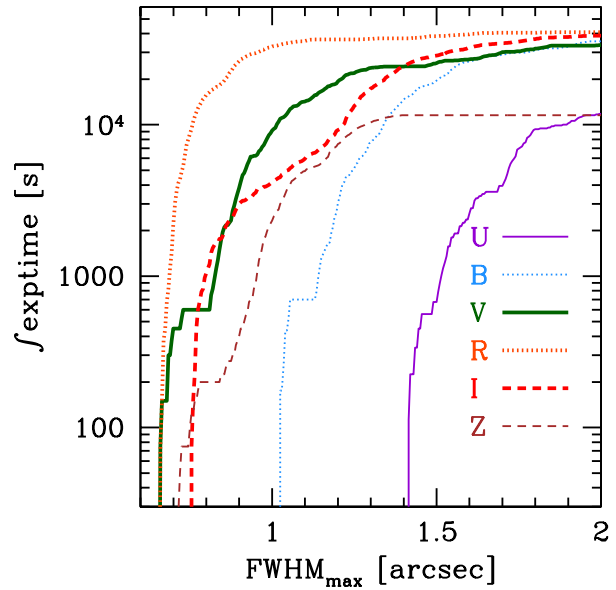


**Figure 2.** Cumulative exposure time as a function of limiting seeing in WFI frames of RXC J2248.7-4431 used in this work. Bold lines show the bands used for shape measurement, where we have applied seeing full-width at half maximum (FWHM) cuts at 0.9 arcsec (1.0 arcsec) in R (V and I) band, respectively.

time as a function of limiting point-spread function (PSF) full-width at half maximum (FWHM) are shown in Figure 2. The excellent depth and seeing in R band (with over 9 hours of exposure time at sub-arcsecond seeing, yielding a coadded image with 0.8 arcsec PSF FWHM and limiting magnitude of  $m_{R,\text{Vega},\text{lim}} = 26.7$  for a  $5\sigma$  detection inside a 1 arcsec diameter aperture) make it our primary lensing band, but also in V (0.9 arcsec seeing with  $m_{V,\text{Vega},\text{lim}} = 26.4$ ) and I band (0.9 arcsec PSF FWHM with  $m_{I,\text{Vega},\text{lim}} = 24.4$ ) shape measurements of background galaxies are feasible.

We perform de-biasing, flat fielding, masking of bad pixels in all bands and fringe pattern correction in the I and Z band using the Astro-WISE<sup>2</sup> pipeline (Valentijn et al. 2007). Background subtraction, final astrometry and co-addition of suitable frames is done externally using SCAMP<sup>3</sup> (Bertin 2006) and SWarp<sup>4</sup> (Bertin et al. 2002). The central part of a colour image based on these co-added frames is shown in Figure 1.

For photometry, we take observations of standard star fields in B, V and R to fit zeropoints for each CCD individually and extinction coefficients globally. From nights which we confirm to be photometric according to their standard star measured zeropoints we build a photometric B, V and R stack. We build deeper stacks including frames from all available nights with relative photometry fitted by SCAMP and match the magnitudes measured from these stacks to the photometric ones in order to find zeropoints for the deep stacks. Alternatively, fixing the R band zeropoint, we find U,

<sup>2</sup> <http://www.astro-wise.org/>

<sup>3</sup> <http://www.astromatic.net/software/scamp>

<sup>4</sup> <http://www.astromatic.net/software/swarp>

<sup>1</sup> <https://www.eso.org/lasilla/instruments/wfi/inst/filters/>

B, V, I and Z zeropoints by minimising residuals in colour-colour diagrams with respect to the stellar library of Pickles (1998). The stellar locus zeropoints found in this way for B and V agree within 0.02 mag with the photometric zeropoints found by matching the two versions of the stacks, confirming that our photometric pipeline provides consistent results.

### 3 PREVIOUS WORK ON RXC J2248.7-4431

The cluster RXC J2248.7-4431 studied in this work is also known as Abell S1063 or MACS 2248-4431. Here we give an overview of all literature on the cluster published previously to this work, including detections and redshift estimates, X-ray observations and SZ measurement. We discuss the more detailed findings of Gómez et al. (2012) and compare them to our own analyses in Section 7.

RXC J2248.7-4431 was first listed by Abell et al. (1989) with a background-corrected galaxy count of 74. It was independently detected by the ROSAT All-Sky Survey (de Grandi et al. 1999), who quote a redshift estimate of  $z = 0.252$ , which was, however, only weakly determined based on the Abell et al. (1989) distance class. Cruddace et al. (2002) give its redshift as  $z = 0.1495$  based on private communications with H. Andernach (1989). Böhringer et al. (2004) finally quote a spectroscopic redshift of  $z_{cl} = 0.3475$ , which is what we adopt for this work. This is confirmed by spectroscopy of 51 cluster members with a mean redshift of  $z = 0.3461^{+0.0010}_{-0.0011}$  (Gómez et al. 2012).

Gómez et al. (2012) find the spectroscopic velocity dispersion of to be  $\sigma_v = 1660^{+230}_{-150} \text{ km s}^{-1}$ , which corresponds to a mass of  $M_{200c} = 42^{+17}_{-9} \cdot 10^{14} M_{\odot}$  according to the relation of Evrard et al. (2008).

Cruddace et al. (2002) quote an X-ray temperature of 7.823 keV from the ROSAT All-Sky Survey (RASS). Maughan et al. (2008) give the X-ray temperature within  $R_{500}$  as  $11.1^{+0.8}_{-0.9} \text{ keV}$  and parametrise the cluster profile as slightly elliptical with  $1 - b/a = 0.2$  based on Chandra ACIS-I data. Both values are based, however, on earlier erroneous cluster redshifts ( $z = 0.1495$  for Cruddace et al. 2002 and  $z = 0.252$  for Maughan et al. 2008). The Planck Collaboration et al. (2011b) quote an X-ray mass based on their follow-up with XMM-Newton of  $M_{500c} = (12.25 \pm 0.21) \cdot 10^{14} M_{\odot}$  which they use to calibrate their SZ MOE. Comis et al. (2011) determine  $M_{2500c} = (5.3 \pm 2.6) \cdot 10^{14} M_{\odot}$  from Chandra X-ray data and Gómez et al. (2012) give a consistent value from independent data reduction of the same data of  $M_{2500c} = (6.0 \pm 1.6) \cdot 10^{14} M_{\odot}$ .

Plagge et al. (2010) parametrise the SZ profile measured with the South Pole Telescope (SPT) with a  $\beta$  parameter of  $(0.86 \pm 0.02)$  arcmin at a scaling of  $\Delta T \approx 1 \text{ mK}$ . Williamson et al. (2011) quote an SZ signal-to-noise ratio (S/N) of 20.7 and a SZ mass of  $M_{200m} = (28.2 \pm_{\text{stat}} 3.6 \pm_{\text{sys}} 9.3) \cdot 10^{14} M_{\odot}$ . The Planck Collaboration et al. (2011a) detect the SZ effect of RXC J2248.7-4431 at  $13.93\sigma$  significance. From the Planck SZ observable and scaling relation (Planck Collaboration et al. 2011b) the SZ mass is  $M_{500c} = (11.5 \pm_{\text{stat}} 2.6 \pm_{\text{sys}} 0.5) \cdot 10^{14} M_{\odot}$ .

Guzzo et al. (2009) and Plagge et al. (2010) show X-ray and SZ imaging of the cluster, respectively. The cluster is

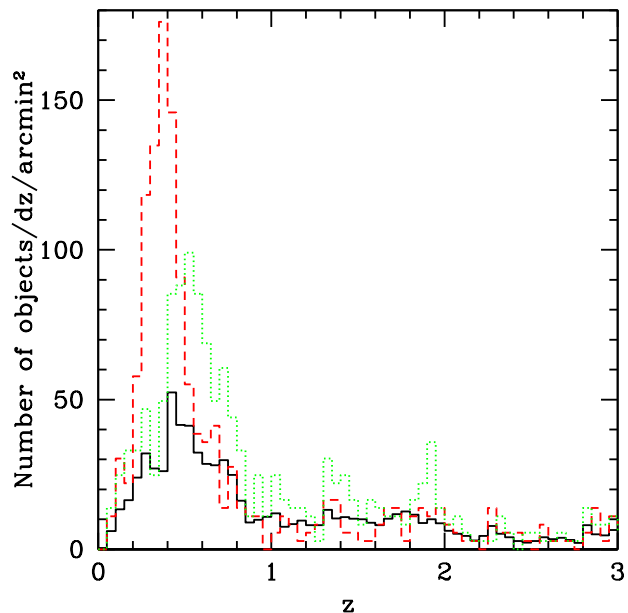


**Figure 3.** Three-dimensional galaxy density as a function of photometric redshift in the WFI field (black, solid lines) and inside a circle of radius 100 arcsec around the brightest cluster galaxy of RXC J2248.7-4431 (red, dashed lines). The cluster at a redshift of  $z_{cl} = 0.3475$  (Böhringer et al. 2004) can be clearly seen as a peak in this smaller field. The green, dotted line shows objects within a radius of 100 arcsec around the BCG of the  $z \approx 0.6$  cluster described in Section 8.

also covered by the CLASH project (Postman et al. 2012; Monna et al. 2013).

## 4 PHOTOMETRIC ANALYSIS

### 4.1 Photometric Redshifts

The multicolour catalogue creation and photometric redshift estimation follows the procedure described in Brimiouille et al. (2013). Here we only give a brief overview. We convolve all data with a Gaussian kernel to match the seeing to the band where it is largest (in this case the U band). This equalisation of the PSF is required for reliable aperture colours in the different filters. We then run SExtractor<sup>5</sup> in dual-image mode to extract fluxes, including weight images and masks of bad areas in the detection and extraction frame. We detect the objects on the unconvolved R-band with a S/N threshold of  $2\sigma$  on at least four contiguous pixels. Flux and magnitude information is extracted from the convolved images. We correct for extinction and zeropoint accuracies by comparing the stellar locus in colour-colour-diagrams to the stellar library of Pickles (1998). We then use the photometric template-fitting algorithm of Bender et al. (2001) to estimate photometric redshifts.

The density of galaxies in redshift space is shown in Figure 3. The cluster is clearly visible as a redshift density

<sup>5</sup> <http://www.astromatic.net/software/sextractor>

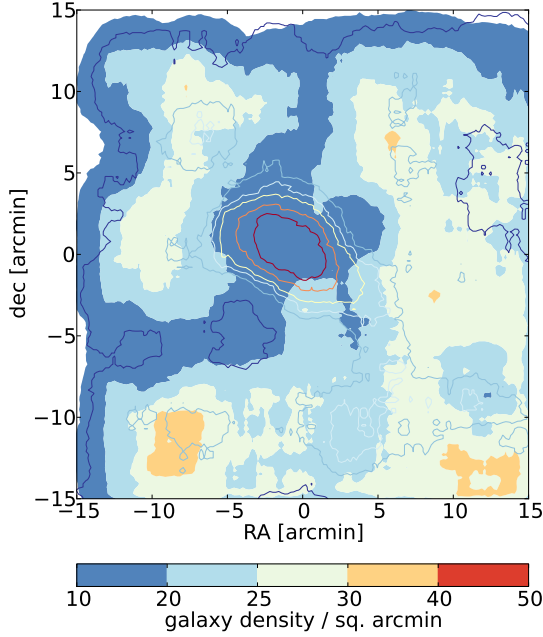


**Figure 4.** Density of galaxies in our photometric redshift catalogue in a map centred on the BCG position, averaged in angular boxes of  $4 \times 4$  arcmin size. Contour lines show density per arcmin<sup>2</sup> per redshift interval for sources with  $|z - z_{\text{cl}}| < 0.04 \cdot (1 + z_{\text{cl}})$ . The background colour shows the overall density of sources above the redshift cut of Eqn. 1. The depletion of background galaxies at the cluster position is an indication that our background sample is pure. The high background density observed in the lower left of the map is due to the system discussed in Section 8.

peak around the spectroscopic  $z_{\text{cl}} = 0.3475$ , which is also true for the second cluster at a mean photometric redshift of  $z \approx 0.6$ , described in detail in Section 8.

In our weak lensing analysis we only consider background galaxies with a minimum photometric redshift of

$$z_{\text{source}} > 1.1 \cdot z_{\text{cl}} + 0.15 \approx 0.53. \quad (1)$$

We include objects up to a maximum photometric redshift of  $z = 4$ . We verify that this excludes redshift mismeasurement of cluster galaxies into the background sample by means of redshift density maps at the cluster redshift and for objects selected by the background cut of Eqn. 1 in Figure 4. Indeed, the cluster is seen as a highly significant overdensity of objects around  $z_{\text{cl}}$ , while the density of background sources near the cluster is smaller than in the field. This is expected owing to the area covered by cluster light and indicates that background contamination is not a significant issue, as expected for the red cluster galaxies whose redshift can be determined photometrically to good accuracy.

#### 4.2 Cluster member SEDs

We investigate photometric properties and spectral energy distribution types (SEDs) of the cluster member galaxies of RXC J2248.7-4431 and the second cluster at  $z \approx 0.6$  (cf. Section 8).

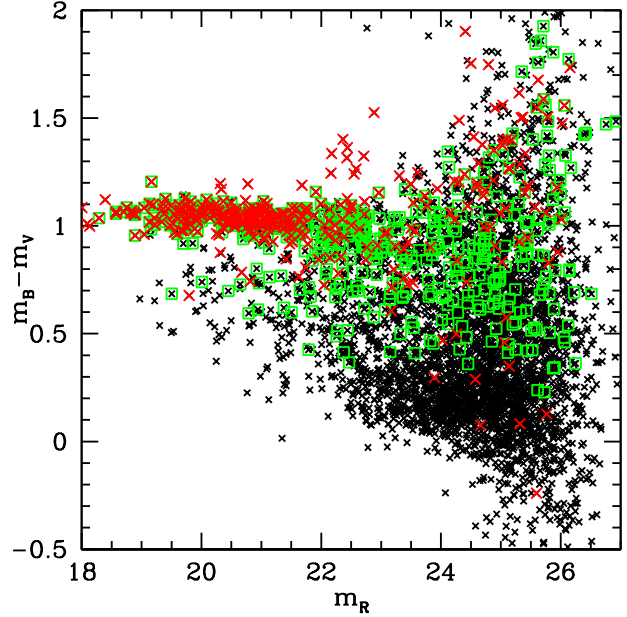


**Figure 5.** Colour-magnitude diagram of galaxies within 5 arcmin projected separation from the BCG, using B-V aperture colours and R band `MAG_AUTO` magnitudes and showing all objects (black, small crosses), objects with red spectral energy distribution types (cf. Dahlen et al. 2005; Brimiouille et al. 2013) (red, large crosses) and marking objects in a redshift slice  $|z - z_{\text{cl}}| \leq 0.04 \cdot (1 + z_{\text{cl}})$  around the cluster by a green open square.

The brightest cluster galaxy (BCG) of RXC J2248.7-4431 has a photometric redshift of 0.4 and an absolute magnitude of  $M_{R,\text{Vega}} = -24.81$ . Its counterpart in the  $z \approx 0.6$  cluster has a photometric redshift of 0.66 and an absolute magnitude of  $M_{R,\text{Vega}} = -25.1$ .

Cluster members galaxies are preferentially of early type and, at a given redshift, lie on a relatively tight sequence in colour-magnitude space, the red sequence. We plot B-V aperture colours, which are particularly indicative of the D4000 break, against R band `MAG_AUTO` magnitudes in Figure 5. The red sequence is clearly detected and dominant among cluster members. We measure the fraction of red galaxies on a sample of cluster members selected by their photometric redshift  $|z - z_{\text{cl}}| \leq 0.04 \cdot (1 + z_{\text{cl}})$  for both RXC J2248.7-4431 and the second cluster found at  $z \approx 0.6$ . Figure 6 shows the fraction of these galaxies which are classified photometrically as having a red SED (cf. Dahlen et al. 2005; Brimiouille et al. 2013),  $N_{\text{red}}/N_{\text{total}}$ , as a function of projected separation from the cluster in units of its  $r_{200m}$  according to our best-fit NFW models (see Sections 6.5 and 8) and as a function of depth.

The latter is fixed relative to the characteristic luminosity of the Schechter function,  $L^*$ , or in this case  $m^*$ , is estimated by fitting a Schechter function to the statistically background corrected cluster luminosity function (as in Zenteno et al. 2011). The limiting depth for the fit is chosen at  $m^* + 4$ , where  $m^*$  is found iteratively. The offset of 4 limits the magnitude range so it is well sampled for both clusters. In this way we find characteristic magnitudes of  $m_{R,\text{Vega}}^* = 19.3^{+0.5}_{-0.6}$  ( $m_{R,\text{Vega}}^* = 22.2^{+0.9}_{-1.7}$  for the  $z \approx 0.6$  cluster) for apparent R band and  $M_{r,\text{AB}}^* = -23.4^{+0.3}_{-0.3}$ .



( $M_{r,AB}^* = -23.9^{+0.9}_{-1.0}$ ) for absolute magnitudes in SDSS r' band.

We conclude that approximately 50 per cent of cluster members are red galaxies near the core of RXC J2248.7-4431, and that this fraction continuously drops towards the outskirts, where it is below 20 per cent. For the higher redshift system, the fraction of red galaxies in the cluster is significantly lower (which is known as the Butcher-Oemler Effect, Butcher & Oemler 1978). The fraction of red galaxies decreases both towards fainter magnitudes, larger separations from the core and higher redshift.

#### 4.3 Mass from richness and luminosity

We can find an independent estimate of cluster mass by means of mass-observable relations of richness and absolute luminosity. To this end, we apply the prescription of Wen et al. (2010). For our cluster member catalogue we select luminous galaxies inside a projected radius of 1Mpc around the BCG within  $|z - z_{cl}| \leq 0.06 \cdot (1 + z_{cl})$  and with magnitudes  $M_{r'} \leq -21$ , where we use absolute magnitudes in SDSS r' band (Gunn et al. 1998). The size and r' band luminosity of the sample is 64 and  $L_{r'} = 3.0 \cdot 10^{12} L_{\odot}$ . After subtracting the mean number and luminosity of similar object selected from a region of the field more than 3Mpc from the BCG, we find a background corrected richness of  $R = 54$  and luminosity of  $L_{r'} = 2.6 \cdot 10^{12} L_{\odot}$ .

Applying the scaling relations of Wen et al. (2010), this yields

$$\begin{aligned} \log M_{101c} / (10^{14} h^{-1} M_{\odot}) &= (-1.57 \pm 0.12) + 1.55 \log R \\ &= 1.12 \pm_{\text{stat}} 0.09 \pm_{\text{sys}} 0.12 \quad (2) \end{aligned}$$

from richness as the mass proxy with systematic and statistical uncertainty. Alternatively, one can use the net luminosity to obtain

$$\begin{aligned} \log M_{101c} / (10^{14} h^{-1} M_{\odot}) &= (-2.03 \pm 0.06) \\ &+ 1.49 \log L_{r'} / (10^{10} h^{-2} L_{\odot}) \\ &= 1.14 \pm_{\text{stat}} 0.09 \pm_{\text{sys}} 0.06 \quad (3) \end{aligned}$$

Since the errors of these two estimates are highly correlated we use the less uncertain Eqn. 3, which yields a mass of  $M_{101c} = 19 \pm 6 \cdot 10^{14} M_{\odot}$ .

## 5 WEAK LENSING MEASUREMENT

Weak gravitational lensing changes the ellipticities of the images of galaxies in the background of massive structures. Its measurement therefore requires the determination of pre-seeing galaxy shapes. In this section we describe our shape measurement, while the analysis of the signal is presented in Section 6.

### 5.1 Model of the Point-Spread Function

Any estimate of the pre-seeing shape of a galaxy requires knowledge of the point-spread function (PSF). For a successful and unbiased weak lensing analysis it is most crucial to model the point-spread function accurately (cf. Kitching et al. 2013), since mismatches in ellipticity and size

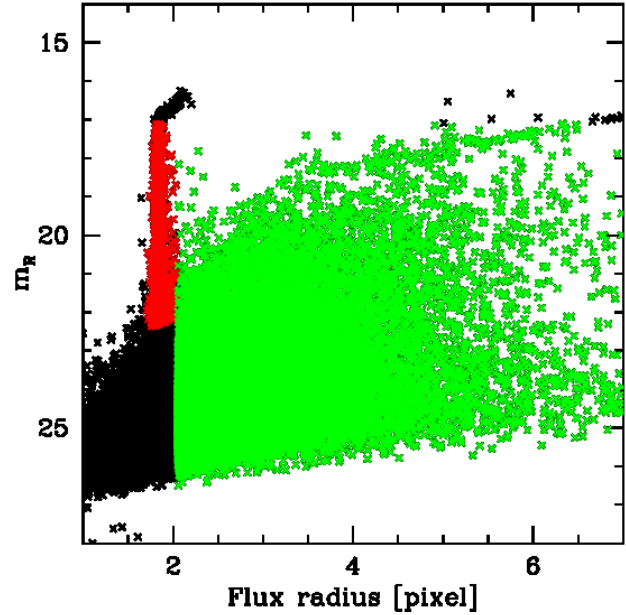


**Figure 7.** Selected stars for PSF modelling (red) and sources initially accepted for shape measurement (green).

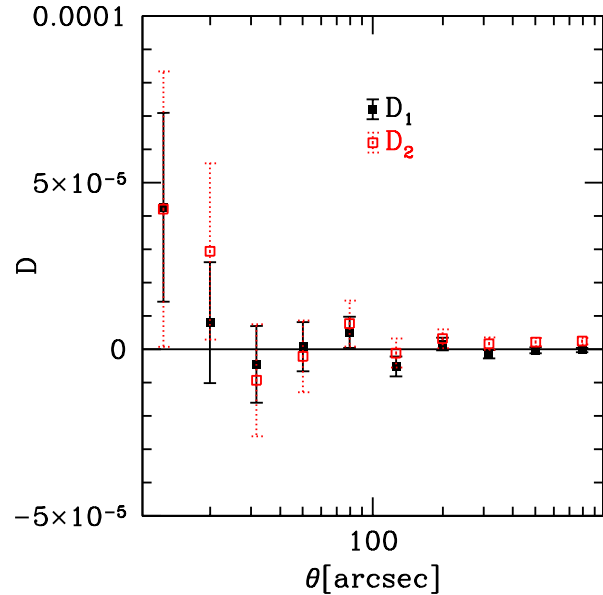


**Figure 8.** Autocorrelation of PSF model ellipticity residuals ( $D_1$ ) and cross-correlation of residuals and measured ellipticity ( $D_2$ ) according to Rowe (2010) for a 5th order polynomial PSF model in the R band co-add. While lower orders show signs of underfitting ( $D_1$  and/or  $D_2$  significantly non-zero on some scales), higher orders do not improve the model further and show signs of overfitting ( $D_2$  significantly negative on some scales).

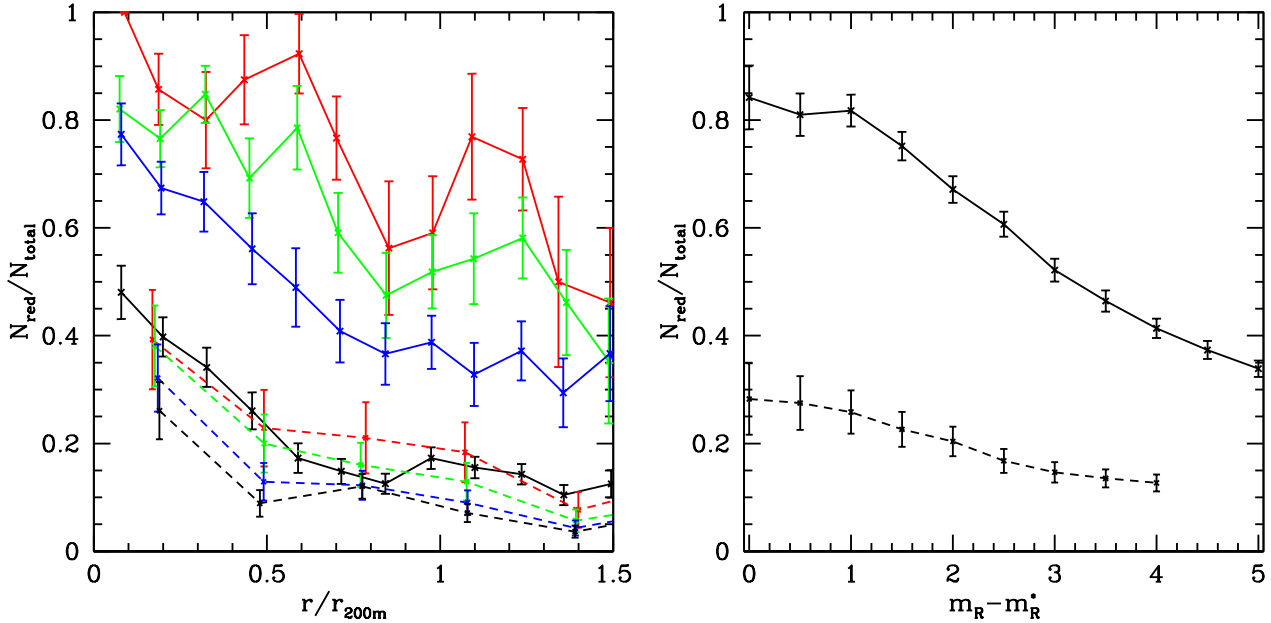


**Figure 6.** Fraction of galaxies having a red SED type in the redshift slice and projected vicinity of RXC J2248.7-4431 (solid lines) and the second cluster at  $z \approx 0.6$  (dashed lines). The left panel shows the red fraction as a function of radius from the BCG in units of  $r_{200m}$  of the respective system with magnitude limits at  $m_R^* + 1$  (red),  $m_R^* + 2$  (green),  $m_R^* + 3$  (blue) and our detection limit (black). The right panel shows the red fraction inside  $r_{200m}$  of the respective system as a function of magnitude limit, which reaches the overall detection limit at  $m_R^{\text{lim}} - m_R^* \approx 4$  for the  $z \approx 0.6$  system. Error bars are calculated from the Poissonian noise in the number counts of red and blue galaxies in each bin.

of the PSF model cause additive and multiplicative systematic errors in the shape estimate, respectively.

We use PSFEx<sup>6</sup> (Bertin 2011) for determining the profile of the PSF as a polynomial function of the position in the co-added focal plane. To this end, we perform a pre-selection of stars according to size, S/N and the SExtractor<sup>7</sup> neural network star classifier (Bertin & Arnouts 1996). The pre-selected stars (cf. Figure 7) are used to determine the PSF model, which is then checked using the following diagnostics:

- mean and scatter of residual ellipticities and sizes to check for remaining offsets and quality of the fit,
- whisker plot of residual ellipticities to exclude failure of the fit in specific regions of the focal plane, and
- two-point autocorrelations of ellipticity residuals ( $D_1$ ) and cross-correlation of residuals and measured star ellipticities ( $D_2$ ) to exclude under- and overfitting, as defined in Rowe (2010), Eqn. 13-14.

We verify, in particular, that a star preselection is necessary for the size of the PSFEx model to match the size of the PSF well enough. In R and V a smooth PSF model over the whole focal plane is a sufficient description of the observed pattern. We find that, similar to other exposures from the WFI camera we have analysed in the past, the I band PSF is more difficult to model. Only when masking the border regions between neighbouring chips and discarding all stars and galaxies in those regions can we describe

the PSF with a simple polynomial dependence on position to sufficient accuracy. For these tests we find that the method of Rowe (2010) is particularly helpful, and use it to determine the correct polynomial order of the spatial variation (5 (7) for the R (V and I) band, respectively), which match the observed PSF without clear signs of over- or underfitting (cf. Figure 8).

## 5.2 Shape Measurement

We run an implementation of the KSB+ method (Kaiser et al. 1995 (KSB), Luppino & Kaiser 1997 and Hoekstra et al. 1998) using the PSFEx PSF model (KSBPSFEx) that has been tested against simulations at intermediate to large tangential shears and proven to be viable in the cluster shear regime (Young et al. 2013). The pipeline includes the following preparation steps for the KSB+ shape measurement:

- unsaturated sources with flux radii larger than the stellar flux radius and zero SExtractor flags are filtered,
- postage stamps of  $64 \times 64$  pix size are extracted and neighbouring objects according to the SExtractor segmentation map are masked,
- the SExtractor photometric background estimate at the object position is subtracted from the image in order to compensate for small-scale background variations insufficiently modelled by the data reduction pipeline,
- bad and masked pixels are interpolated using a Gauss-Laguerre model of the galaxy (Bernstein & Jarvis 2002), where we discard objects with more than 20 per cent of

<sup>6</sup> <http://www.astromatic.net/software/psfex>

<sup>7</sup> <http://www.astromatic.net/software/sextractor>

postage stamp area or 5 per cent of model flux falling onto bad or masked pixels.

As the final step of the shape measurement, KSB+ is run on the cleaned postage stamp of the galaxy and the sub-pixel resolution PSF model at the galaxy position. For details, we refer the reader to the papers introducing and extending the method. Here we only give a brief summary.

KSB measure polarisations

$$\mathbf{e} = \frac{1}{Q_{11} + Q_{22}} \begin{pmatrix} Q_{11} - Q_{22} \\ 2Q_{12} \end{pmatrix} \quad (4)$$

using second moments calculated inside a Gaussian aperture,

$$Q_{ij} = \int d^2\theta I(\boldsymbol{\theta}) w(|\boldsymbol{\theta}|) \theta_i \theta_j, \quad (5)$$

of the surface brightness distribution of the galaxy  $I(\boldsymbol{\theta})$  with a Gaussian weight function  $w(|\boldsymbol{\theta}|)$  centred on the galaxy centroid. In our implementation, the weight function for measuring the galaxy and PSF moments is scaled with the measured half-light radius of the observed galaxy.

Cluster weak lensing analyses require the ensemble measurement of reduced shear (cf. Bartelmann & Schneider 2001, p.60). In the presence of an elliptical PSF, the linear approximation of how observed post-seeing polarisation  $\mathbf{e}_o$  reacts to a reduced shear  $\mathbf{g}$  can be expressed as

$$\mathbf{e}_o = \mathbf{e}_i + \hat{P}^{\text{sm}} \mathbf{p} + \hat{P}^\gamma \mathbf{g}, \quad (6)$$

where  $\mathbf{e}_i$  is the intrinsic post-seeing ellipticity of the galaxy,  $\hat{P}^{\text{sm}}$  is a  $2 \times 2$  tensor quantifying the response of observed shear to PSF polarisation  $\mathbf{p}$  and  $\hat{P}^\gamma$  is the shear responsivity tensor. Inverting  $(\hat{P}^\gamma)^{-1} \approx \frac{2}{\text{tr} P^\gamma}$  and assuming that  $(\hat{P}^\gamma)^{-1} \mathbf{e}_i$  is zero on average because of the random intrinsic orientation of galaxies, this yields the ensemble shear estimate

$$\langle \mathbf{g} \rangle = \langle \boldsymbol{\epsilon} \rangle = \left\langle \frac{2}{\text{tr} P^\gamma} \mathbf{e}_o - \hat{P}^{\text{sm}} \mathbf{p} \right\rangle. \quad (7)$$

We remove objects with failed KSB+ measurements and objects with  $\text{tr} P^\gamma < 0.1$  from the final shape catalogue. The latter is a requirement owing to the noisiness of measured  $\text{tr} P^\gamma$ , which otherwise greatly amplifies the uncertainty of Eqn. 7 (cf. Applegate et al. 2012; Newman et al. 2013; Schrabback et al. 2007; Romano et al. 2010, for similar clipping schemes at various levels of  $\text{tr} P^\gamma$ ). We match R, V and I band shape catalogues and take the arithmetic mean of all available bands as the individual object shape and match against the photometric redshift catalogue to select valid background galaxies and assign redshift scalings. This and the S/N cut introduced in Section 5.3 leaves us with an average of 9 galaxies per square arcminute in the background of RXC J2248.7-4431 with a mean ratio of angular diameter distances of  $\langle D_{ds}/D_s \rangle = 0.59$  (cf. Section 6.1).

### 5.3 Noise Bias Calibration

Biases of shape estimators are commonly expressed as a multiplicative and an additive term (Heymans et al. 2006), where the additive component is typically due to imperfect correction for the ellipticity of the PSF. The latter effect is particularly relevant for cosmic shear analyses, where

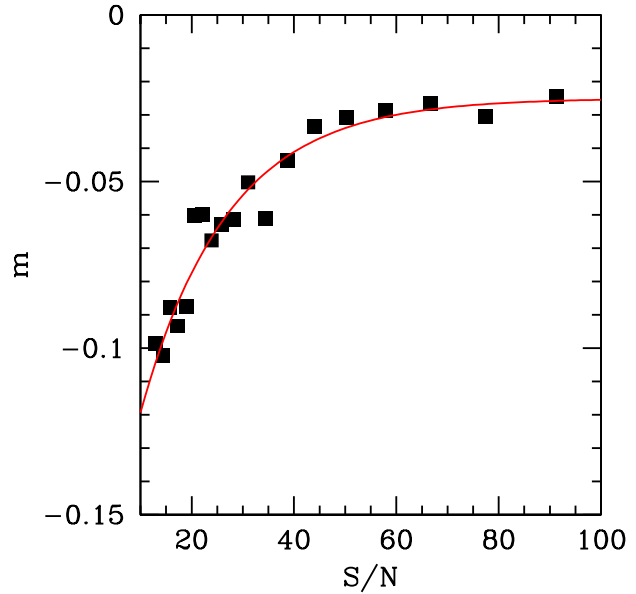


**Figure 9.** Multiplicative bias  $m$  as a function of signal-to-noise ratio (S/N) for our shape pipeline, as measured using image simulations with a range of PSF sizes, shears and galaxy properties typical for a weak lensing cluster study like ours. The results are well-fit by Eqn. 9 with best-fitting parameters  $A = 0.025$ ,  $B = 0.17$  and  $C = 17$  (red line).

auto-correlations of the shear field are calculated and auto-correlations of the PSF ellipticity field would enter the equation by means of an additive bias (for a more detailed study of the influence of shape biases on cosmic shear, see Amara & Réfrégier 2008). All analyses we do in this cluster weak lensing study, however, deal with shear estimates averaged in an annulus, in which case any constant additive bias cancels out. Pixel noise, on the contrary, typically causes multiplicative biases at the per-cent level over a wide range of observational conditions, which would directly enter our cluster weak lensing model (Melchior & Viola 2012). This and the fact that we do not observe significant additive biases on simulated images with elliptical PSF is the reason for limiting our calibration to the most important factor, namely noise dependent multiplicative bias.

Shape measurement, primarily because it involves division by noisy quantities, suffers from a noise bias, which is negligible for bright galaxies but becomes troublesome for the faint end of background galaxies in a weak lensing analysis (Kaiser 2000; Bernstein & Jarvis 2002; Melchior & Viola 2012; Refregier et al. 2012; Kacprzak et al. 2012). Many studies in the past have applied a global correction factor to their KSB shape catalogue (see Clowe et al. 2012; Schrabback et al. 2007; Newman et al. 2013; Ragozzine et al. 2012 for a range of factors used), but there also have been cases where calibration has been matched to galaxy S/N and sometimes also size using simulated galaxy images (Schrabback et al. 2010; von der Linden et al. 2012). We quantify the magnitude of noise bias in our pipeline using image simulations with a range of PSF sizes, shears and galaxy properties typical for a weak lensing cluster study like ours (Young et al. 2013).

If a shear estimator  $g_o$  only has multiplicative bias  $m$ , it can be written as

$$g_o = (1 + m) \cdot g + N, \quad (8)$$

where  $g$  is the true shear and  $N$  is a noise term with zero mean. We fit  $m$  for simulated sets of galaxies and show the results in Figure 9 as a function of S/N measured according to the prescription of (Erben et al. 2001). The multiplicative bias is fit well by the functional form

$$m = -A - B \cdot \exp(-(S/N)/C) \quad (9)$$

with best-fit values of  $A = 0.025$ ,  $B = 0.17$  and  $C = 17$  down to a signal-to-noise ratio of 10.

We discard objects outside the regime this calibration was tested on (i.e. where  $S/N < 10$  (Erben et al. 2001) or  $(S/N)_{\text{iso}} < 15$  as measured inside an isophotal aperture of  $1.5\sigma$  significance per pixel over the background). The remainder of our sample is calibrated with the  $m$  of Eqn. 9, by multiplying shape estimates by a factor of  $1/(1 + m(S/N))$ .

## 6 WEAK LENSING ANALYSIS

### 6.1 Introduction

Cluster weak lensing analysis aims to reconstruct properties of the density field of clusters of galaxies from the reduced shear they impose on the images of background galaxies. We refer the reader to the review of Bartelmann & Schneider (2001) for an in-depth introduction and only give a brief overview of the main concepts here.

Gravitational shear  $\gamma$  relates to reduced shear  $g$  as

$$\gamma = g \cdot (1 - \kappa), \quad (10)$$

where  $\kappa$  is the projected surface mass density in units of the critical surface density,  $\kappa = \Sigma/\Sigma_c$ , with

$$\Sigma_c = \frac{c^2}{4\pi G} \frac{D_s}{D_d D_{ds}}. \quad (11)$$

The latter contains a geometric factor composed of angular diameter distances  $D_{s,d,ds}$  from observer to source, from observer to lens and from lens to source, respectively.

The surface mass density is related to the mean tangential component of the shear on a circle,  $\gamma_t(r)$ , by the simple equation

$$\gamma_t(r) = \langle \kappa(< r) \rangle - \kappa(r), \quad (12)$$

the difference between mean  $\kappa$  inside and on the edge of the circle.

Equations 10 and 12 show that the observable  $g$  is invariant under mass sheet transformations,  $\kappa \rightarrow \lambda\kappa + (1 - \lambda)$ , a degeneracy which can be broken for instance by assuming a functional form of  $\kappa(r)$ .

In the following we use two common density profiles, the singular isothermal sphere (SIS) and the NFW profile (Navarro et al. 1996). Their densities are given by

$$\rho_{\text{SIS}}(r) = \frac{\sigma_v^2}{2\pi G r^2}, \quad (13)$$

with a constant velocity dispersion  $\sigma_v$ , and

$$\rho_{\text{NFW}}(r) = \frac{\rho_0}{(r/r_s) \cdot (1 + r/r_s)^2}. \quad (14)$$

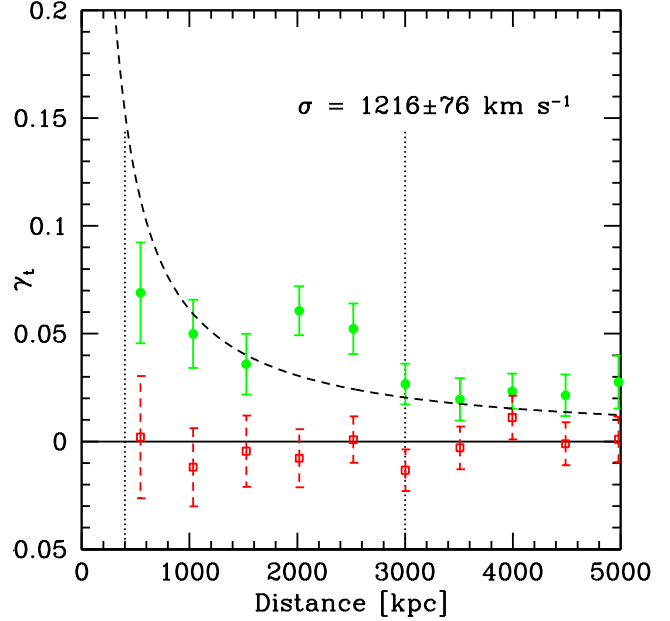


**Figure 10.** Tangential alignment (green circles), B mode (red squares) and singular isothermal sphere fit (dashed line) inside the interval delimited by dotted vertical lines. Note that the B mode is consistent with 0 as expected for a bias-free shape catalogue.

The NFW profile has two free parameters which are commonly expressed in terms of the mass and concentration  $c_{\Delta m} = r_{\Delta m}/r_s$  or  $c_{\Delta c} = r_{\Delta c}/r_s$  instead of the central density  $\rho_0$  and the scale radius  $r_s$  used in the equation above.

The projected surface mass density and tangential shear profiles of a SIS can be readily integrated as

$$\kappa(r) = \gamma_t(r) = 2\pi \left( \frac{\sigma_v}{c} \right)^2 \frac{D_{ds}}{D_s} \frac{1}{r}. \quad (15)$$

For the NFW profile, we refer the reader to the calculations in Wright & Brainerd (2000).

### 6.2 Tangential Alignment

We first measure the tangential alignment signal around the brightest cluster galaxy (cf. Fig. 10). For this we calculate the mean reduced tangential shear  $g_t$  in radial bins and convert it into tangential gravitational shear  $\gamma_t$  assuming a singular isothermal sphere (SIS) profile, for which (cf. Eqns. 10 and 15)

$$\gamma_t = \frac{g_t}{1 + g_t}. \quad (16)$$

The effective distance ratio  $D_{ds}/D_s$  is calculated from the mean individual galaxy values in each bin. The SIS fit yields a velocity dispersion of  $\sigma_v = 1216 \pm 76 \text{ km s}^{-1}$ , measuring in the radial range of 400 to 3000 kpc projected distance. As it follows from Eqn. 13,

$$r_{200c} = \frac{\sqrt{2}\sigma_v}{10H(z)} = (2025 \pm 126) \text{ kpc} \quad \text{and} \quad (17)$$

$$r_{200m} = \frac{\sqrt{2}\sigma_v}{10H_0 \sqrt{\Omega_m} \cdot (1+z)^3} = (2979 \pm 184) \text{ kpc}, \quad (18)$$



which implies a mass of  $M_{200c,SIS} = (14.0 \pm 2.6) \times 10^{14} M_{\odot}$  and  $M_{200m,SIS} = (21.0 \pm 3.8) \times 10^{14} M_{\odot}$ .

### 6.3 Significance Map

For a first two-dimensional view of the lensing signal, we measure the surface mass density or, equivalently, tangential gravitational shear inside circular weighted apertures, so-called aperture masses (Schneider 1996). We show the significance of aperture masses above zero as a function of position in Figure 11. For this we use a Gaussian weight function

$$w(|\boldsymbol{\theta}|) \propto \begin{cases} \exp(-|\boldsymbol{\theta}|^2/(2\sigma_w^2)) & |\boldsymbol{\theta}| < 3\sigma_w \\ 0 & \text{otherwise} \end{cases} \quad (19)$$

to calculate the significance, defined as the ratio between aperture mass and its uncertainty,  $M_{ap}/\sigma_{M_{ap}}$  (Bartelmann & Schneider 2001, their Sec. 5.3 and Schirmer et al. 2004), with

$$M_{ap}(\boldsymbol{\theta}) = \sum_i w(|\boldsymbol{\theta} - \boldsymbol{\theta}_i|) \cdot g_{i,t}$$

$$\sigma_{M_{ap}} = \sqrt{\frac{1}{2} \sum_i w^2(|\boldsymbol{\theta} - \boldsymbol{\theta}_i|) \cdot |g_i|^2}, \quad (20)$$

where  $g_{i,t}$  is the tangential reduced shear of galaxy  $i$  measured with respect to  $\boldsymbol{\theta}$ . For the width of the aperture we use  $\sigma_w = 3 \text{ arcmin}$ . We detect the cluster as a peak in the aperture significance map with a significance of  $5\sigma$ , centred on the BCG with a deviation of only few arcseconds. The significance map indicates an anisotropic distribution of mass around its centre, with additional peaks towards the north-eastern, south-western and southern direction from the BCG. We also check the significance of aperture B-mode peaks and find them to be consistent with a random field.

### 6.4 Mass Density Map

We calculate a density map using the method of Kaiser & Squires (1993). For this we use all sources that satisfy the background cut of Eqn. 1. These sources have a mean ratio of angular diameter distances of  $\langle D_{ds}/D_s \rangle = 0.59$ . The  $\kappa$  map has a pixel size of 1 arcmin and is smoothed with a Gaussian of  $\sigma = 1.2 \text{ arcmin}$  width. The map is shown in Figure 12 for the full field of view.

### 6.5 NFW Model

We further perform a likelihood analysis (see Schneider et al. 2000) for a two-parametric NFW profile (Navarro et al. 1996) of the halo, fitting the concentration parameter  $c_{200m}$  and the mass  $M_{200m}$  simultaneously. We use background galaxies above a projected separation of 1 Mpc at the cluster redshift, since inside this limit some of the tested models predict shear above the weak regime and, in addition, astrophysical effects near the core of the cluster disturb the expected signal most (cf. Mandelbaum et al. 2010). This justifies the assumption of a model-independent dispersion of intrinsic shapes in Eqn. 15 of Schneider et al. (2000). We use  $\sigma_{\epsilon} = 0.3$ , the dispersion of our best-fit subtracted shape residuals, and determine confidence limits using the  $\Delta\chi^2$  statistics of Avni (1976).

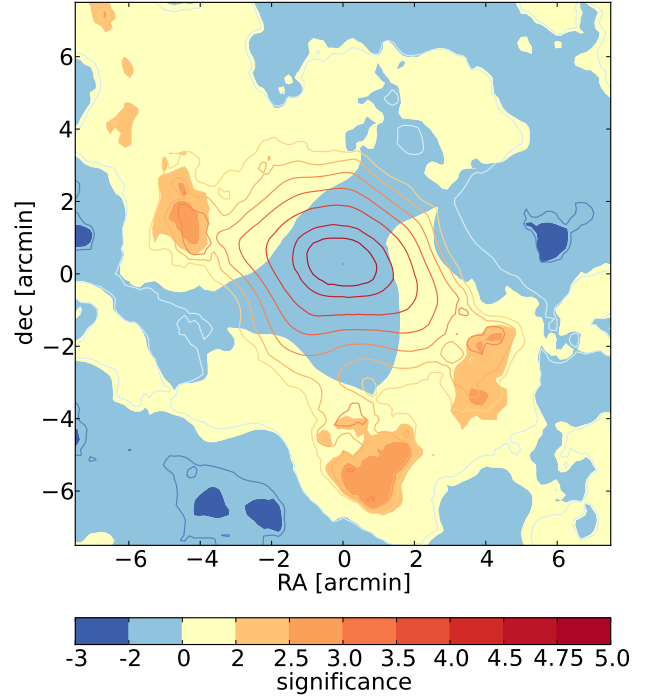
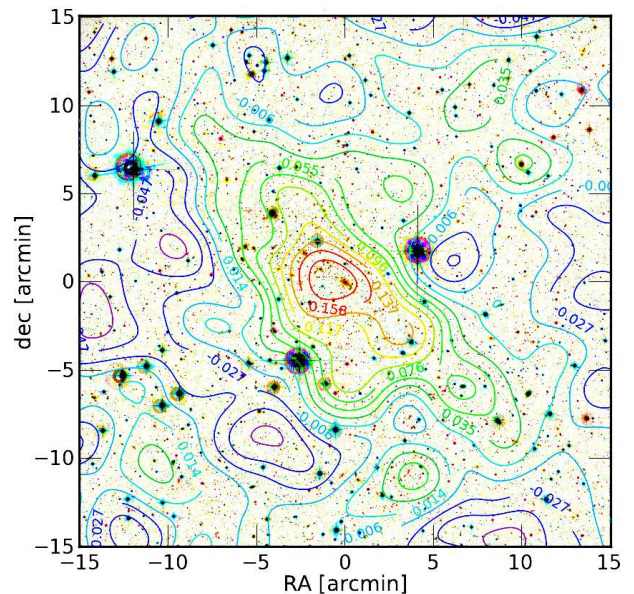


**Figure 11.** Aperture mass significance map calculated according to Eqns. 19 and 20. Contour lines show the significance of aperture mass measured on background galaxies according to the cut of Eqn. 1, which is centred on the BCG at a significance of  $5\sigma$ . The background colour shows the aperture mass significance of the residual shape catalogue after subtracting the best fit NFW model of the central halo (cf. Section 6.5). Towards the lower left is the south-eastern corner of the image.



mass definition	our NFW fit	literature value	source	method
$M_{200m}$	$33.1^{+9.6}_{-6.8}$	$28.2 \pm_{\text{stat}} 3.6 \pm_{\text{sys}} 9.3$	Williamson et al. (2011)	SZ
$M_{101c}$	$32.2^{+9.3}_{-6.6}$	$19 \pm 6$	this work, Section 4.3, and Wen et al. 2010	luminosity
$M_{200c}$	$22.8^{+6.6}_{-4.7}$	$42^{+17}_{-9}$	Gómez et al. (2012)	kinematics
$M_{500c}$	$12.7^{+3.7}_{-2.6}$	$12.25 \pm 0.21$	Planck Collaboration et al. (2011b)	X-ray / XMM-Newton
		$11.5 \pm_{\text{stat}} 2.6 \pm_{\text{sys}} 0.5$	Planck Collaboration et al. (2011b)	SZ
$M_{2500c}$	$2.8^{+0.8}_{-0.6}$	$5.3 \pm 2.6$	Comis et al. (2011)	X-ray / Chandra

**Table 1.** Best fit mass and confidence region of our NFW model ( $M_{200m}$ ) converted to other definitions of mass inside spherical overdensity using the best fit concentration of  $c_{200m} = 2.6$ . All values are given in units of  $10^{14} M_{\odot}$ .

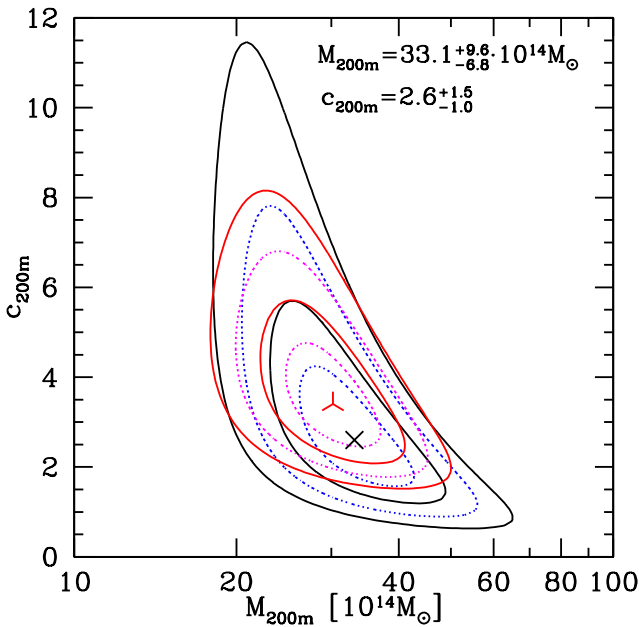


**Figure 13.** Likelihood contours of the two-parametric NFW profile of RXC J2248.7-4431. Black, solid (blue, dotted) contours show the combined (projected) confidence regions (intervals) for  $M_{200m}$  and  $c_{200m}$  with no concentration prior. Red, solid (magenta, dotted) contours for the combined (projected) confidence regions (intervals) using the concentration prior of Bullock et al. (2001); Duffy et al. (2008). All contours are drawn at the  $1\sigma$  and  $2\sigma$  confidence levels. The black cross (red triangular symbol) indicate the best-fit solution without (with) concentration prior.

The  $1\sigma$  confidence limits for mass and concentration individually are  $M_{200m} = 33.1^{+9.6}_{-6.8} \cdot 10^{14} M_{\odot}$ ,  $c_{200m} = 2.6^{+1.5}_{-1.0}$ , where because of a degeneracy the very high masses only occur at unlikely low concentrations. Confidence contours are shown in Figure 13.

Since there is prior knowledge about the concentration of dark matter haloes at given mass and redshift, we can reduce the uncertainty of our measurement by multiplying the likelihood with a concentration term

$$p(c|M, z) = e^{-(\log c - \log c(M, z))^2 / (2\sigma_{\log c}^2)} \quad (21)$$

where we adopt the mass-concentration relation  $c(M, z)$  of Duffy et al. (2008) and a lognormal distribution of concentrations according to Bullock et al. (2001) with  $\sigma_{\log c} = 0.18$ .

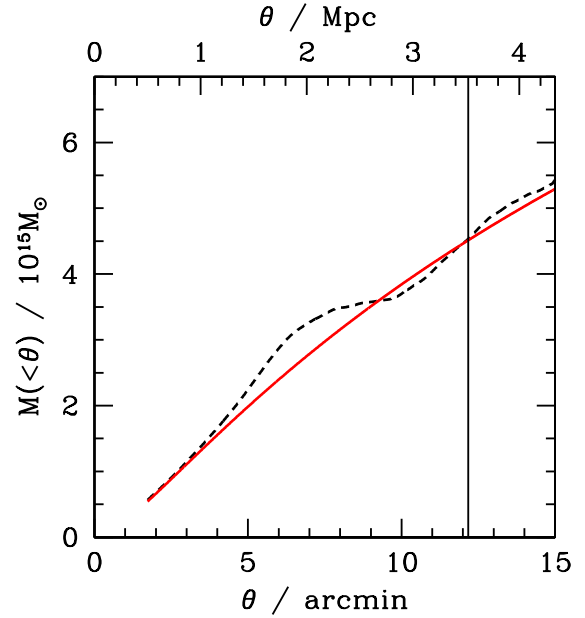


**Figure 14.** Projected excess mass inside a circle around the BCG of RXC J2248.7-4431, shown for the best-fit NFW model (red, solid line) and directly measured from the observed tangential shear profile (black, dashed line), fixed at  $r_{200m}$  (vertical line).

This leads to confidence limits of  $M_{200m} = 30.2^{+6.1}_{-5.1} \cdot 10^{14} M_{\odot}$  and  $c_{200m} = 3.4^{+1.3}_{-0.9}$ .

For reference and comparison, we give corresponding masses in different definitions of spherical overdensity in Table 1. Our result is consistent inside the error limits with the X-ray mass of the Planck Collaboration et al. (2011b) and the SZ masses of Williamson et al. (2011) and Planck Collaboration et al. (2011b). The X-ray mass at high overdensity of Comis et al. (2011) is higher than our best fit, yet relatively uncertain and likely dominated by highly concentrated baryonic matter in and around the BCG, which is not correctly modelled by a global NFW halo. The mass calculated from richness and luminosity in Section 4.3 is significantly lower than our weak lensing result, yet likely contains systematic uncertainties because it was calibrated with different data. Spectroscopic velocity dispersion of cluster members yields a significantly higher mass estimate (Gómez et al. 2012), discussed in more detail in Section 7.

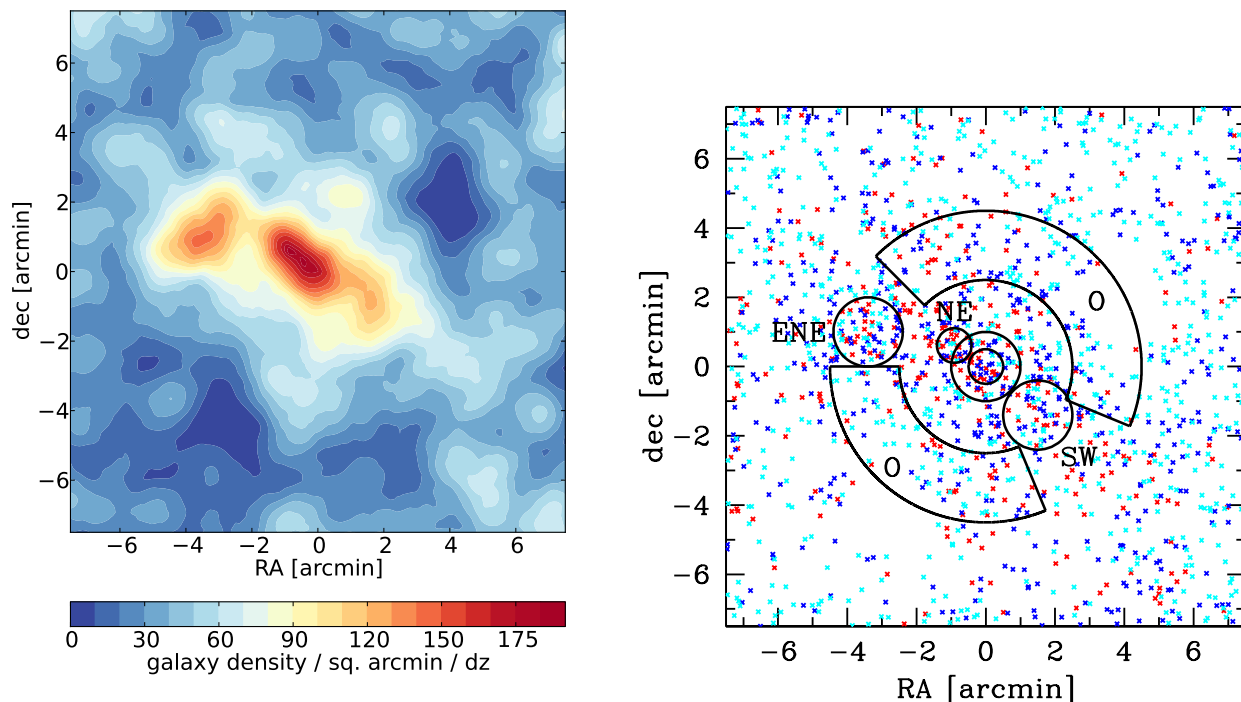


**Figure 15.** Left panel: Density of galaxies with  $|z - z_{cl}| < 0.06 \cdot (1 + z_{cl})$  in our photometric redshift catalogue centred on the BCG position, measured as a kernel density with the minimum-variance (Epanechnikov) kernel of 1 arcmin radius. Right panel: Positions of red (red), moderately star-forming Sb/c-like (blue) and star-forming (cyan) galaxies around the centre of RXC J2248.7-4431 in the same redshift slice. The areas delineated by black lines indicate the regions used for the SED analysis in Table 2. The two empty regions visible at radii of  $\approx 5$  arcmin from the center correspond to positions of bright stars and their associated masks.

In addition, we plot mass enclosed in a cylinder of varying radius, centred on the BCG, in Figure 14.

Deviations from the spherically symmetrical NFW profile are known to exist in several different forms, such as correlated secondary haloes, asphericity of the main halo or filamentary structures (Dietrich et al. 2012b) and can influence the accuracy of weak lensing cluster analyses significantly (Gruen et al. 2011). In order to investigate these effects, we plot the aperture mass significance map on a shape catalogue with the signal of the best-fit model subtracted in Figure 11. While the central peak is described well by the spherical profile, we find that there are additional peaks towards the north-eastern, south-western and southern direction from the BCG, with the northern one potentially highly elongated towards the north-north-east. This is in line with the density map (cf. Section 6.4) and the shape of the galaxy concentration in three dimensional space (cf. Fig. 4). These structures therefore most likely represent correlated structures physically close to the main halo of RXC J2248.7-4431.

## 7 ON THE HYPOTHESIS OF A RECENT MERGER IN RXC J2248.7-4431

Gómez et al. (2012) present evidence for a recent merger of RXC J2248.7-4431 based on optical imaging, spectroscopy of 51 cluster members and analysis of the X-ray emission of

peak	$N_{gal}$	red [%]	mod. SF [%]	SF [%]
central 1'	78	$41 \pm 6$	$41 \pm 6$	$18 \pm 4$
ENE	67	$33 \pm 6$	$37 \pm 6$	$30 \pm 6$
SW	50	$32 \pm 7$	$36 \pm 7$	$32 \pm 7$
O	239	$22 \pm 3$	$36 \pm 3$	$42 \pm 3$
central 0.5'	29	$48 \pm 9$	$41 \pm 9$	$11 \pm 6$
NE	29	$51 \pm 9$	$28 \pm 8$	$21 \pm 8$

**Table 2.** Fractions of galaxies by SED type for the galaxy density peaks identified in Section 7.1 and shown in Table 2.

the system. We briefly recollect their findings and compare them with our results from deeper images with photometric redshift information and weak lensing.

### 7.1 Galaxy number density

The cluster member number density, selected either based on spectroscopic redshift or in colour-magnitude space, is found by Gómez et al. (2012) to be multimodal (their Figures 7-9). We study the projected density of galaxies in the region of the cluster in Figure 15. The multimodality is confirmed, where the two peaks of Gómez et al. (2012) form a

highly elongated central region of approximately 2 arcmin diameter. An additional peak towards the east-northeastern (ENE) direction (not inside the field of view of the images used by Gómez et al. 2012) and a less dense but still visible peak towards the southwestern (SW) direction (also identified by Gómez et al. (2012), but below their significance threshold).

Our mean photometric redshifts of galaxies inside a cylinder of 1 arcmin radius around all three peaks are mutually consistent with each other and with the spectroscopic mean cluster redshift. The uncertainty of the ensemble mean of  $\delta z \approx 0.005$  for each peak, however, would only allow a significant detection of peculiar motions of several  $1000 \text{ km s}^{-1}$  along the line of sight.

Comparing the galaxy density map with Figure 11, we find a rough correspondence of the two galaxy density sub-peaks with the two residual peaks in the aperture mass significance after subtracting the best-fit model for the central halo. The third significant additional aperture significance peak towards the south does not correspond to a structure clearly visible in the galaxy number density.

## 7.2 Galaxy SEDs

We examine the distributions of best-fitting SED types from the photometric redshift code for the galaxy density peaks identified in Gómez et al. (2012) and in the previous section. To this end, we select galaxies inside cylindrical volumes of 1 arcmin (0.5 arcmin) radius and  $|z - z_{cl}| < 0.06 \cdot (1 + z_{cl})$  around the three peaks (and the two central peaks of Gómez et al. 2012). Results are shown in Figure 15 and Table 2, discriminating red, moderately star-forming Sb/c-like and star-forming SEDs.

The galaxy populations in the ENE and SW peak contain a smaller fraction of red galaxies than in the very centre of the cluster, yet a larger one than elsewhere at similar separation from the BCG (in the region labelled O).

Even if their distance from the centre in three dimensions is higher than in projection, the latter observation cannot be explained by the environmental influence of the core of RXC J2248.7-4431 alone and indicates that ENE and SW are evolved neighbouring structures in the outskirts of a major cluster.

For the two peaks identified by Gómez et al. (2012), the galaxy populations are too small to make significant statements about differences in SED distribution (cf. Table 2, central 0.5 arcmin and NE).

## 7.3 Centroid offsets

Gómez et al. (2012) note an offset between the BCG and the centroid of X-ray emission when measuring the latter on larger radii. We note that the point of highest significance of the lensing signal (cf. Fig 11) is less than 20 arcsec off the BCG, which is consistent with the random offsets expected from shape noise (cf. Dietrich et al. 2012a). The strong lensing model of RXC J2248.7-4431 (Monna et al. 2013) also shows no offset between the central galaxy and the peak of the projected density field.

## 7.4 Discrepancy between lensing and other mass estimates

Weak lensing mass estimates are not influenced by the astrophysical state of a system, unlike estimates based on the dynamic state of cluster members or the intra-cluster gas. Therefore a discrepancy between weak lensing and other mass estimates could suggest the influence of dynamic astrophysical processes such as mergers. Gómez et al. (2012) hypothesise that a lensing mass significantly lower than the dynamical and X-ray masses found for RXC J2248.7-4431 could help confirm merger activity.

The mass calculated by Gómez et al. (2012) based on the velocity dispersion of cluster members is slightly inconsistent with our weak lensing mass on the high side ( $M_{200c}^{\text{dyn}} = 42_{-9}^{+17} \cdot 10^{14} M_{\odot}$  versus  $M_{200c}^{\text{WL}} = 22.8_{-4.7}^{+6.6} \cdot 10^{14} M_{\odot}$ ), indicating that opposite bulk motion of different galaxy populations along the line of sight could be present. Whether there is indeed substructure in the velocity fields of the cluster members, for which Gómez et al. (2012) find marginal evidence will be investigated in detail with the forthcoming VLT-CLASH large spectroscopic programme (P. Rosati, private communication).

We see no significant discrepancy, however, of weak lensing with X-ray or SZ mass estimates of the cluster. Gómez et al. (2012) find an inconsistency between masses inside 110 kpc apertures from X-ray modelling in hydrostatic equilibrium and a strong lensing model. The latter, however, is based on a candidate multiply imaged system identified in their relatively shallow photometry which deeper observations have revealed to be not from the same source (Monna et al. 2013). At this point, there is therefore also no compelling evidence of a discrepancy between lensing and X-ray mass estimates in the core of RXC J2248.7-4431.

## 7.5 Influence of neighbouring structures on lensing mass

We attempt to quantify the influence of the structures in the environment of RXC J2248.7-4431 on its weak lensing mass estimate by fitting a model with multiple haloes to the observed shear signal. To this end, we place two haloes with fixed concentration-mass relation (Duffy et al. 2008) at the position of the BCG and the centre of the east-northeastern peak (cf. Section 7.1). The confidence region for the mass of the secondary peak is in this case  $M_{200m}^{\text{ENE}} = 4.2_{-1.9}^{+2.2} \cdot 10^{14} M_{\odot}$ . Subtracting the best-fitting model of the secondary peak and fitting the central halo of RXC J2248.7-4431 with two free parameters yields  $M_{200m} = 24.0_{-5.8}^{+6.1} \cdot 10^{14} M_{\odot}$  and  $c_{200m} = 2.8_{-1.2}^{+3.0}$ . The corresponding mass for comparison with other estimates is  $M_{500c} = 9.6_{-2.3}^{+2.5} \cdot 10^{14} M_{\odot}$ .

We note that this lower mass of the central peak is still in agreement with the SZ and X-ray masses listed in Table 1. It is unclear whether or not the mass of the secondary peak should in fact be included in a  $M_{200m}$  estimate of RXC J2248.7-4431 since the projected separation of 3.5 arcmin is well below  $r_{200m}$  of the central system. While this exemplifies the sensitivity of cluster weak lensing to correlated structures (Gruen et al. 2011), it does not change the conclusions of Section 7.4.



## 8 SECONDARY CLUSTER AT $z \approx 0.6$

In redshift space density maps we detect a secondary peak around  $(\alpha, \delta) = (22^{\text{h}}49^{\text{m}}37.1^{\text{s}}, -44^{\circ}43'04'')$ , at the position of a bright early-type galaxy with photometric redshift of  $z = 0.66$  and corresponding absolute rest-frame magnitude of  $M_{R,\text{Vega}} = -25.1$  which appears to be at the centre of another cluster of galaxies. At a separation of 14.5 arcmin from the centre of RXC J2248.7-4431, this configuration of lenses is significantly more separated than the cases of cluster-cluster-lensing discussed in Zitrin et al. (2012). In the following, we present a weak lensing and a simple strong lensing analysis of the newly discovered cluster.

The mean redshift of the 12 closest, visually colour-selected member galaxies is  $z = 0.58$ , which is the redshift we use for the following weak lensing analysis. After subtracting the best-fit NFW model of the central peak of RXC J2248.7-4431 (cf. Section 6.5), we model this structure as an NFW halo positioned on the BCG using the concentration prior of Eqn. 21 and a radial range of  $0.5 \text{ Mpc} \leq r \leq 3 \text{ Mpc}$ . The confidence contours are shown in Figure 16. As a result of the low background number density and location of the cluster near the edge of the image, the mass is only weakly constrained and not detected at the  $2\sigma$  level. We find the confidence region to be  $M_{200m} = 4.0^{+3.7}_{-2.6} \cdot 10^{14} M_{\odot}$  at a concentration of  $c_{200m} = 4.3^{+2.2}_{-1.4}$ . Owing to the lack of completeness at the required depth, a richness and luminosity derived mass estimation (cf. Section 4.3) is not feasible. Figure 17 shows a colour image of the central part of the system.

We identify four blue sources in a cross-like orientation around the BCG with separations of  $\sim 8$  arcsec and  $\sim 17$  arcsec along the small and large axis, respectively, as a candidate of multiple imaging. Assuming a cluster redshift of  $z_l = 0.58$ , the redshift of the blue source at its photometric value of  $z_s = 1.58$ , and a halo with projected ellipticity and orientation following the light distribution of the BCG, we can build a strong lensing model. For a nonsingular halo with 4 arcsec (27 kpc) core radius, we get a mass of  $\sim 1.4 \cdot 10^{13} M_{\odot}$  within a radius of 6.8 arcsec, the Einstein radius at this redshift.

## 9 CONCLUSIONS

We present the first weak lensing analysis of the cluster of galaxies RXC J2248.7-4431. We calculate photometric redshifts of background and cluster galaxies and determine the richness and total luminosity of the system. We find the mass and concentration of RXC J2248.7-4431 in a NFW likelihood analysis to be equal to  $M_{200m} = 33.1^{+9.6}_{-6.8} \cdot 10^{14} M_{\odot}$ , in good agreement with previous X-ray and SZ mass estimates, and  $c_{200m} = 2.6^{+1.5}_{-1.0}$ , which is in the lower range of expected concentration for a system of the given mass and redshift. The subtraction of the best-fitting model leaves three marginally significant aperture mass peaks in the vicinity of the main halo, which likely correspond to substructure and surrounding structures of RXC J2248.7-4431. We confirm and add to some of the evidence given by Gómez et al. (2012) for an ongoing major merger of the system in terms of the multimodal galaxy density field and a discrepancy between (low) weak lensing and (high) dynamical mass estimate. We do not,

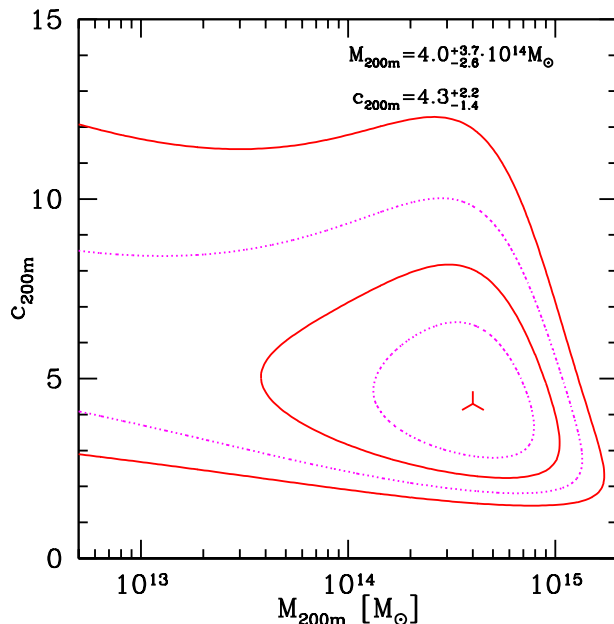


**Figure 16.** Likelihood contours of the two-parametric NFW profile of secondary cluster with  $z = 0.58$ . Red, solid (magenta, dotted) contours for the combined (projected) confidence regions (intervals) for  $M_{200m}$  and  $c_{200m}$  using the concentration prior of Bullock et al. (2001); Duffy et al. (2008). Both contours are drawn at the  $1\sigma$  and  $2\sigma$  confidence levels. The triangular symbol indicates the best-fit solution.

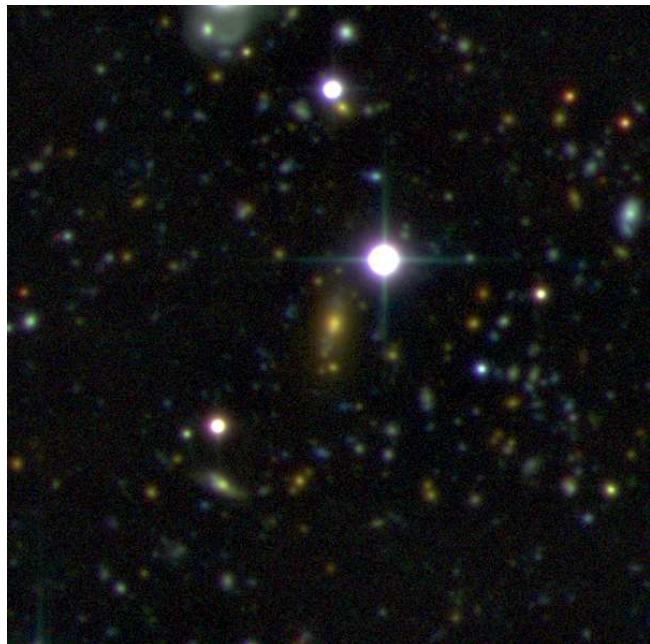


**Figure 17.** Colour image of second cluster at  $(\alpha, \delta) = (22^{\text{h}}49^{\text{m}}37.1^{\text{s}}, -44^{\circ}43'04'')$ ,  $z \approx 0.6$ , with a size of  $2 \times 2$  arcmin. Note the redder colour of BCG and cluster member galaxies compared to RXC J2248.7-4431 (cf. Figure 1) and the four symmetric blue sources along the major and minor axes of the BCG (the former ones highly blended with the BCG itself) at  $z_{\text{phot}} \approx 1.5 \dots 1.8$ .

however, find a tension between X-ray hydrostatic masses and the weak lensing mass of the cluster. This remains to be true even when a secondary peak of galaxy density at 3.5 arcmin separation of the core of RXC J2248.7-4431 is independently included in the weak lensing model.

We detect a second cluster at  $z \approx 0.6$  inside our field of view, whose weak lensing mass is weakly constrained at  $M_{200m} = 4.0^{+3.7}_{-2.6} \cdot 10^{14} M_{\odot}$  with a concentration of  $c_{200m} = 4.3^{+2.2}_{-1.4}$ . In this system a strong lensing analysis of a candidate multiply imaged source is possible.

## ACKNOWLEDGEMENTS

This work was supported by SFB-Transregio 33 ‘The Dark Universe’ by the Deutsche Forschungsgemeinschaft (DFG) and the DFG cluster of excellence ‘Origin and Structure of the Universe’. The authors thank Megan Donahue, August E. Evrard and the anonymous referee for useful comments on the manuscript. VV thanks Bhuvnesh Jain for helpful discussions.

## REFERENCES

- Abell G. O., Corwin, Jr. H. G., Olowin R. P., 1989, *ApJS*, 70, 1
- Allen S. W., Schmidt R. W., Fabian A. C., 2002, *Mon. Not. Roy. Astron. Soc.*, 334, L11
- Amara A., Réfrégier A., 2008, *Mon. Not. Roy. Astron. Soc.*, 391, 228
- Applegate D. E. et al., 2012, *ArXiv e-prints*
- Avni Y., 1976, *ApJ*, 210, 642
- Bartelmann M., Schneider P., 2001, *Physics Reports*, 340, 291
- Battye R. A., Weller J., 2003, *Phys. Rev. D*, 68, 083506
- Bender R. et al., 2001, in *Deep Fields*, Cristiani S., Renzini A., Williams R. E., eds., p. 96
- Bernstein G. M., Jarvis M., 2002, *AJ*, 123, 583
- Bertin E., 2006, in *Astronomical Society of the Pacific Conference Series*, Vol. 351, *Astronomical Data Analysis Software and Systems XV*, Gabriel C., Arviset C., Ponz D., Enrique S., eds., p. 112
- Bertin E., 2011, in *Astronomical Society of the Pacific Conference Series*, Vol. 442, *Astronomical Data Analysis Software and Systems XX*, Evans I. N., Accomazzi A., Mink D. J., Rots A. H., eds., p. 435
- Bertin E., Arnouts S., 1996, *A&AS*, 117, 393
- Bertin E., Mellier Y., Radovich M., Missonnier G., Didelon P., Morin B., 2002, in *Astronomical Society of the Pacific Conference Series*, Vol. 281, *Astronomical Data Analysis Software and Systems XI*, Bohlender D. A., Durand D., Handley T. H., eds., p. 228
- Böhringer H. et al., 2004, *A&A*, 425, 367
- Brimioulle F., Seitz S., Lerchster M., Bender R., Snigula J., 2013, *ArXiv e-prints*, 1303.6287v1
- Bullock J. S., Kolatt T. S., Sigad Y., Somerville R. S., Kravtsov A. V., Klypin A. A., Primack J. R., Dekel A., 2001, *Mon. Not. Roy. Astron. Soc.*, 321, 559
- Butcher H., Oemler, Jr. A., 1978, *ApJ*, 219, 18
- Clowe D., Markevitch M., Bradač M., Gonzalez A. H., Chung S. M., Massey R., Zaritsky D., 2012, *ApJ*, 758, 128
- Comis B., de Petris M., Conte A., Lamagna L., de Gregori S., 2011, *Mon. Not. Roy. Astron. Soc.*, 418, 1089
- Craddace R. et al., 2002, *ApJS*, 140, 239
- Dahlen T., Mobasher B., Somerville R. S., Moustakas L. A., Dickinson M., Ferguson H. C., Giavalisco M., 2005, *ApJ*, 631, 126
- de Grandi S. et al., 1999, *ApJ*, 514, 148
- Dietrich J. P., Böhnert A., Lombardi M., Hilbert S., Hartlap J., 2012a, *Mon. Not. Roy. Astron. Soc.*, 419, 3547
- Dietrich J. P., Werner N., Clowe D., Finoguenov A., Kitching T., Miller L., Simionescu A., 2012b, *Nat*, 487, 202
- Duffy A. R., Schaye J., Kay S. T., Dalla Vecchia C., 2008, *Mon. Not. Roy. Astron. Soc.*, 390, L64
- Erben T., Van Waerbeke L., Bertin E., Mellier Y., Schneider P., 2001, *A&A*, 366, 717
- Evrard A. E. et al., 2008, *ApJ*, 672, 122
- Gómez P. L. et al., 2012, *AJ*, 144, 79
- Gruen D., Bernstein G. M., Lam T. Y., Seitz S., 2011, *Mon. Not. Roy. Astron. Soc.*, 416, 1392
- Gunn J. E. et al., 1998, *AJ*, 116, 3040
- Guzzo L. et al., 2009, *A&A*, 499, 357
- Haiman Z., Mohr J. J., Holder G. P., 2001, *ApJ*, 553, 545
- Heymans C. et al., 2006, *Mon. Not. Roy. Astron. Soc.*, 368, 1323
- Hoekstra H., Donahue M., Conselice C. J., McNamara B. R., Voit G. M., 2011, *ApJ*, 726, 48
- Hoekstra H., Franx M., Kuijken K., Squires G., 1998, *ApJ*, 504, 636
- Holder G., Haiman Z., Mohr J. J., 2001, *ApJ*, 560, L111
- Hu W., 2003, *Phys. Rev. D*, 67, 081304
- Kacprzak T., Zuntz J., Rowe B., Bridle S., Refregier A., Amara A., Voigt L., Hirsch M., 2012, *Mon. Not. Roy. Astron. Soc.*, 427, 2711
- Kaiser N., 2000, *ApJ*, 537, 555
- Kaiser N., Squires G., 1993, *ApJ*, 404, 441
- Kaiser N., Squires G., Broadhurst T., 1995, *ApJ*, 449, 460
- Kitching T. D. et al., 2013, *ApJS*, 205, 12
- Luppino G. A., Kaiser N., 1997, *ApJ*, 475, 20
- Majumdar S., Mohr J. J., 2004, *ApJ*, 613, 41
- Mandelbaum R., Seljak U., Baldauf T., Smith R. E., 2010, *Mon. Not. Roy. Astron. Soc.*, 405, 2078
- Maughan B. J., Jones C., Forman W., Van Speybroeck L., 2008, *ApJS*, 174, 117
- Melchior P., Viola M., 2012, *Mon. Not. Roy. Astron. Soc.*, 424, 2757
- Monna et al., 2013, in *prep*
- Navarro J. F., Frenk C. S., White S. D. M., 1996, *ApJ*, 462, 563
- Newman A. B., Treu T., Ellis R. S., Sand D. J., Nipoti C., Richard J., Jullo E., 2013, *ApJ*, 765, 24
- Okabe N., Zhang Y., Finoguenov A., Takada M., Smith G. P., Umetsu K., Futamase T., 2010, *ApJ*, 721, 875
- Pickles A. J., 1998, *PASP*, 110, 863
- Piffaretti R., Arnaud M., Pratt G. W., Pointecouteau E., Melin J.-B., 2011, *A&A*, 534, A109
- Plagge T. et al., 2010, *ApJ*, 716, 1118
- Planck Collaboration et al., 2011a, *A&A*, 536, A8
- Planck Collaboration et al., 2011b, *A&A*, 536, A11
- Postman M. et al., 2012, *ApJS*, 199, 25

- Ragozzine B., Clowe D., Markevitch M., Gonzalez A. H., Bradač M., 2012, *ApJ*, 744, 94
- Refregier A., Kacprzak T., Amara A., Bridle S., Rowe B., 2012, *Mon. Not. Roy. Astron. Soc.*, 425, 1951
- Romano A. et al., 2010, *A&A*, 514, A88
- Rowe B., 2010, *Mon. Not. Roy. Astron. Soc.*, 404, 350
- Sahlen M. et al., 2009, *Mon. Not. Roy. Astron. Soc.*, 397, 577
- Schirmer M., Erben T., Schneider P., Wolf C., Meisenheimer K., 2004, *A&A*, 420, 75
- Schneider P., 1996, *Mon. Not. Roy. Astron. Soc.*, 283, 837
- Schneider P., King L., Erben T., 2000, *A&A*, 353, 41
- Schrabback T. et al., 2007, *A&A*, 468, 823
- Schrabback T. et al., 2010, *A&A*, 516, A63
- Sunyaev R. A., Zel'dovich Y. B., 1972, *Comments on Astrophysics and Space Physics*, 4, 173
- Valentijn E. A. et al., 2007, in *Astronomical Society of the Pacific Conference Series*, Vol. 376, *Astronomical Data Analysis Software and Systems XVI*, R. A. Shaw, F. Hill, & D. J. Bell, ed., p. 491
- von der Linden A. et al., 2012, *ArXiv e-prints*
- Wang L., Steinhardt P. J., 1998, *ApJ*, 508, 483
- Weller J., Battye R. A., Kneissl R., 2002, *Phys. Rev. Lett.*, 88, 231301
- Wen Z. L., Han J. L., Liu F. S., 2010, *Mon. Not. Roy. Astron. Soc.*, 407, 533
- Williamson R. et al., 2011, *ApJ*, 738, 139
- Wright C. O., Brainerd T. G., 2000, *ApJ*, 534, 34
- Young et al., 2013, in prep
- Zenteno A. et al., 2011, *ApJ*, 734, 3
- Zitrin A. et al., 2012, *Mon. Not. Roy. Astron. Soc.*, 420, 1621